Journal of Materials Chemistry C

Accepted Manuscript

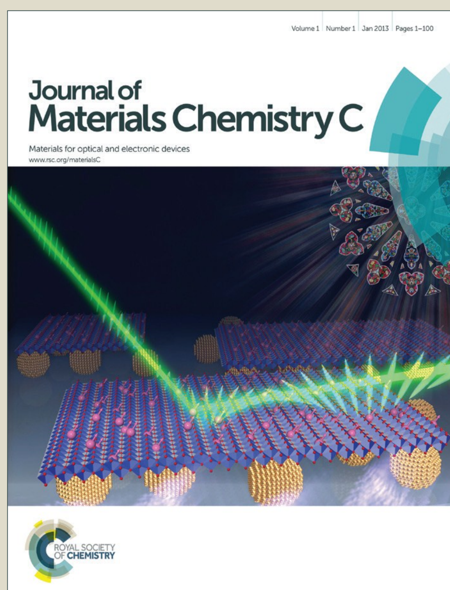

This is an *Accepted Manuscript*, which has been through the Royal Society of Chemistry peer review process and has been accepted for publication.

Accepted Manuscripts are published online shortly after acceptance, before technical editing, formatting and proof reading. Using this free service, authors can make their results available to the community, in citable form, before we publish the edited article. We will replace this *Accepted Manuscript* with the edited and formatted *Advance Article* as soon as it is available.

You can find more information about *Accepted Manuscripts* in the Information for Authors.

Please note that technical editing may introduce minor changes to the text and/or graphics, which may alter content. The journal's standard Terms & Conditions and the Ethical guidelines still apply. In no event shall the Royal Society of Chemistry be held responsible for any errors or omissions in this *Accepted Manuscript* or any consequences arising from the use of any information it contains.

ROYAL SOCIETY OF CHEMISTRY

www.rsc.org/materialsC

Toward high thermoelectric performance *p*-type $FeSb_{2.2}Te_{0.8}$ via *in situ* formation of InSb nanoinclusions

Gangjian Tan[1], Hang Chi[2], Wei Liu[2], Yun Zheng[1], Xinfeng Tang[1,*], Jian He[3], and Ctirad Uher[2]

[1]State Key Laboratory of Advanced Technology for Materials Synthesis and Processing, Wuhan University of Technology, Wuhan 430070, China

[2]Department of Physics, University of Michigan, Ann Arbor, Michigan 48109, United States

[3]Department of Physics and Astronomy, Clemson University, Clemson, South Carolina 29634, United States

Journal of Materials Chemistry C Accepted Manuscript

[*] Correspondences that should be addressed: tangxf@whut.edu.cn

Abstract

We synergistically optimized the thermoelectric properties of *p*-type skutterudite $FeSb_{2.2}Te_{0.8}$ via a facile "electron-channel phonon-barrier" nanocompositing approach *without* invoking the conventional "filling-rattling" concept. The InSb nanoinclusions formed *in situ* at the grain boundaries of *p*-type $FeSb_{2.2}Te_{0.8}$ are playing multiple roles: the high carrier mobility of InSb mitigates the mobility degradation at the grain boundaries (in line with "electron-channel") while the added grain boundaries effectively scatter heat-carrying phonons (in line with "phonon-barrier"). As a result, the simultaneous carrier mobility enhancement and the lattice thermal conductivity reduction yield a high figure of merit ZT of ~ 0.76 at 800 K in the 3 mol.% InSb-containing $FeSb_{2.2}Te_{0.8}$ sample, outperforming any other unfilled p-type skutterudites reported so far. The interplay between the *p*-type $FeSb_{2.2}Te_{0.8}$ host matrix and the *n*-type InSb nanoinclusions was analyzed in view of their respective electronic band structures and also in the context of an effective medium model. These results confirm not only the feasibility of fabricating *p*-type skutterudite nanocomposites but also the great promise of $FeSb_{2.2}Te_{0.8}$ as the *p*-leg material in large-scale production of skutterudite-based thermoelectric modules.

***Keywords*:** p-type skutterudites; thermoelectric property; nanocomposites

Journal of Materials Chemistry C Accepted Manuscript

1. Introduction

Filled MX_3 (M = transition metal element Co, Fe, and X = pnictogen element P, As, and Sb) skutterudites are an archetype of "*phonon-glass electron-crystal*" thermoelectric (TE) material that holds great promise in applications of intermediate temperature power generation.[1-4] For a practical TE module, it is generally preferred that the *p*-leg and *n*-leg materials possess similar chemical composition, mechanical properties, and TE performance, similar to the case of Bi_2Te_3.[5, 6] However, the value of the dimensionless figure of merit (ZT) of *p*-type skutterudites[7-10] is inferior to their *n*-type skutterudite counterparts[3, 11]: the highest ZT value is ~ 1.7-2.0 in *n*-type skutterudite[3, 11] while only about 1.1-1.3 in *p*-type skutterudites[8-10, 12-14]. Such ZT mismatch partially arises from the fact that the "filling-rattling" approach proved very effective with *n*-type skutterudites but less so with *p*-type skutterudites. Hence, the pursuit of higher performance *p*-type skutterudites hinges upon novel approaches that go beyond the traditional "filling-rattling" approach. To this end, the formation of nanocomposite materials holds much promise.

Actually the nanocomposite approach naturally derives from the "filling-rattling" approach. In skutterudites, the covalent bonding is responsible for the high carrier mobility but it also gives rise to an undesirably high lattice thermal conductivity.[15-17] To date, the most effective way of suppressing the lattice thermal conductivity without degrading the carrier mobility significantly is to utilize the "rattling" effect by "filling" voids in the skutterudite structure by appropriate guest atoms.[1-3, 18] While the physical nature of the "rattling effect" is still under debate,[19] single-filling,[20-22]

Journal of Materials Chemistry C Accepted Manuscript

double-filling[23-25] and even triple-filling[3] have been demonstrated. However, as effective as the "filling-rattling" approach is, it has inherent limitations regarding the amount of the filler atom the structure can accommodate. Since each MX_3 unit cell contains 32 atoms but merely two voids are available, there is a restriction on the number of the filler atoms. Moreover, since filling is an exceptionally effective *n*-type doping (filler species enter as cations with electrons going to the conduction band), not all available void sites can be occupied as the structure becomes saturated. The so-called filling fraction limits (FFL) for various filler species have been determined[26]. Exceeding the FFL leads to the formation of secondary phase(s). Notably, secondary phases in the form of nanoinclusions distributed at grain boundaries of the skutterudite matrix were found to be thermoelectrically favorable on several occasions.[9, 27-29]

Inspired by these successes, in this work we adopt an *in-situ* nanocompositing approach in *p*-type skutterudites without invoking the traditional "filling-rattling" concept. A successful implementation of this strategy requires a proper selection of the host matrix and the nanoconstituents since usually nanostructuring would interrupt both the electron and phonon transport[30, 31]. Here we choose coarse grained $FeSb_{2.2}Te_{0.8}$ as the host matrix for the following reasons. In our recent work with Ge-doped[32] and Te-doped[33] *p*-type $FeSb_3$, we demonstrated that, in comparison to $CoSb_3$, an extra heavy hole band near the top of the valence band gave rise to a high *p*-type Seebeck coefficient. In addition, Ge or Te doping on the Sb-site not only optimized the electronic density of states near the Fermi level but also introduced

Journal of Materials Chemistry C Accepted Manuscript

point defects that effectively scattered heat-carrying phonons at elevated temperatures. As a result, a maximum *ZT* value of ~ 0.5 and ~ 0.65 was attained in Ge-doped and Te-doped $FeSb_3$, respectively. These *ZT* values are among the best obtained in *unfilled* *p*-type skutterudites.

Here, InSb is intentionally chosen as the nanoconstituent on account of its excellent electronic properties. First, the analysis of the electrical and thermal transport data of Te-doped *p*-type $FeSb_3$ samples[20] showed that the carrier mobility was degraded upon doping while the lattice thermal conductivity remained high. InSb is known for its exceptionally high carrier mobility[34-36] so its presence should mitigate the interfacial-scattering-induced mobility degradation (so called 'electron-channel'). In addition, the presence of nano-sized inclusions of InSb will result in numerous interfaces in the host matrix and assist in the formation of a multi-scale "hierarchical architecture"[37] that effectively scatters a broad range of heat-carrying phonons (so called 'phonon-barrier'). Second, the InSb nanoinclusions form easily *in situ* when an excess of In is added to the recipe for the skutterudite synthesis. *In situ* formed grain boundaries are generally more coherent than the *ex situ* formed ones, thus favoring high carrier mobility[27, 29, 38, 39]. Finally, pristine InSb tends to exhibit *n*-type behavior,[36] so the present work provides an opportunity to study the electronic interplay between the *p*-type $FeSb_{2.2}Te_{0.8}$ coarse grained host matrix and *n*-type InSb nanoinclusions and thus helps complete the study of InSb as a nanoinclusion in both n-type[24, 27, 38] and p-type host matrix. It should be mentioned here that there was recently a study on p-type skutterudite and n-type InSb composite system.[40] However,

Journal of Materials Chemistry C Accepted Manuscript

Journal of Materials Chemistry C Accepted Manuscript

therein the size of InSb impurity phase is too large (~2 microns) to be called nano-size. In addition, the materials studied therein contain many other undesired phases like $FeSb_2$ and Sb. These would mask or even eliminate the beneficial effects of InSb on the thermoelectric properties of the host material. We hope the 'electron-channel phonon-barrier' concept proposed in this study can be universally applied in other thermoelectric system for better performance.

2. Experimental procedure

The samples with the nominal composition of $FeSb_{2.2}Te_{0.8}$ containing x mol.% InSb (x = 0, 1, 3, 6 and 10) were prepared by a melting-annealing-spark-plasma-sintering procedure. Elemental Fe (99.5%, shot), Sb (99.9999%, ingot), Te (99.99%, ingot) and In (99.99%, shot) were properly weighed according to the nominal compositions and loaded and sealed in an evacuated (~10^{-3} Pa) quartz tube. The mixture was slowly heated to 1373 K, rested there for 24 h and then quenched in a saltwater bath. Subsequently, the ingots were annealed at 823 K for 168 h. The ingots were then ground into fine powders and spark plasma sintered at 803 K for 5 min under the uniaxial pressure of 40 MPa into dense pellets with the diameter of 15 mm. The pellets were sliced into $8 \times 8 \times 1.5$ mm^3 square sheets and $3 \times 2 \times 12$ mm^3 bars for further TE characterization. We note that skutterudites and InSb are both of cubic structure and TE properties of the samples are thus considered to be isotropic.

The phase purity and chemical composition of the as-prepared samples were inspected by powder X-ray diffraction (XRD) on a PANalytical X'Pert Pro X-ray

diffraction system (Cu K_α radiation, λ = 1.5406 Å) and by electron probe microanalysis (EPMA, JXA-8230®, JEOL). Micro-morphologies were investigated using a field emission scanning electron microscopy (FESEM, Hitachi: S-4800) and high-resolution transmission electron microscopy (HRTEM; JEM-2100F).

Low temperature transport properties, including the electrical conductivity (σ), the thermal conductivity (κ) and the Hall coefficient (R_H) were carried out in home-built systems at the University of Michigan. The effective carrier concentration (N_p) was estimated using the relationship $N_p = 1/eR_H$, where e is the elemental charge. The Hall mobility (μ_H) was calculated using the relationship $\mu_H = \sigma R_H$. The high temperature electrical conductivity (σ) and the Seebeck coefficient (α) were measured on a ZEM-1® (Ulvac Riko, Inc.) under a low pressure inert gas (He) atmosphere from 300 to 800 K. The high temperature thermal conductivity (κ) was calculated from the measured thermal diffusivity (D), the specific heat (C_p), and the mass density (d) using the relationship $\kappa = DC_pd$. The thermal diffusivity was measured by the laser flash method on a Netzsch LFA 457 system, and the specific heat (C_p) was measured on a TA® DSC Q20. The density was determined by the Archimedes method and relative densities of all samples are higher than 96%. The lattice thermal conductivity κ_L is estimated by subtracting the electronic part κ_C from κ using the Wiedemann-Franz relationship $\kappa_C=L\sigma T$ with L being the Lorenz number. For skutterudites, $L=2\times10^{-8}$ V^2/K^2 is a well-accepted value.[7, 8, 25] Uncertainties in the electrical conductivity, the Seebeck coefficient, and the thermal conductivity are within 5%, 2%, and 5%, respectively, primarily originating from sample dimension

Journal of Materials Chemistry C Accepted Manuscript

measurements.

3. Results and discussion

3.1 Phase purity, composition, and micromorphology

The data presented in this section were taken on spark plasma sintered samples, if not otherwise noted. Figure 1 shows the powder XRD patterns of $FeSb_{2.2}Te_{0.8}$ - x mol.% InSb samples (hereafter denoted by the "x = 1-10 sample"). In addition to a well indexed skutterudite phase, small amounts of the InSb phase are detected in the x ≥ 3 samples but *not* in the x = 0 sample nor in the x = 1 sample. For the x = 10 sample, some Sb phase is detected. Table 1 summarizes the actual composition of the host matrix determined by EPMA and the relative densities at room temperature for all samples. As clearly seen, the actual compositions match well with the nominal compositions, while the actual In contents are a bit lower than the nominal ones. Besides, all samples have high relative packing densities above 96% and with a variance of 2%, hence the impact of the porosity is expected to be small when we compare TE transport properties among the samples.

Figure 2 displays the FESEM images of the samples. All samples are highly dense without noticeable pores or cracks, consistent with the results of the Archimedes' measurement. Moreover, all samples have a similar matrix grain size below 5 μm. For the pristine sample (the x = 0 "InSb-free" sample shown in Fig. 2(a)), the grains and the grain boundaries are clean, while one starts to see a few sub-10 nm nanoinclusions at grain boundaries of the x = 1 sample (highlighted by red circles in

Journal of Materials Chemistry C Accepted Manuscript

Fig. 2(b)). With a further increase in x, an increasing number of nanoinclusions are observed at grain boundaries (Figs. 2(c), (d) and (e)). Fig. 2(f) shows an area in the x = 3 sample, where nanoinclusions with sizes below 50 nm decorate the grain boundaries. Figures 2(a)-(f) clearly present *in situ* formed nanoparticles.

More microstructural details and elemental mapping for the x = 3 sample are shown in Fig. 3. While elemental mapping of Fe (Fig. 3(b) and Te (Fig. 3(e)) show highly uniform dispersions, this is *not* so for In and Sb. In particular, the grain boundaries (see the areas highlighted by the dotted white line in Fig. 3(a)) are rich in In (Fig. 3(c)) but poor in Sb (Fig. 3(e)). Coupled with the XRD results (Fig. 1), we conclude that the secondary phase dispersing at the grain boundaries is InSb. Figure 3(f) is a schematic diagram of the microstructure, featured by fairly evenly distributed InSb nanoinclusions at the grain boundaries of $FeSb_{2.2}Te_{0.8}$.

HRTEM was employed to confirm the details of nanoinclusions. Figure 4(a) shows some nanoinclusions with the grain size of a few dozens of nm at grain boundaries of the x = 3 sample, in good agreement with FESEM observations. Furthermore, Fig. 4(b) displays an image of an enlarged area in Fig. 4(a), and a high-magnification TEM image inset in Fig. 4(b) shows the interplanar spacing of 0.228 nm, a good match for the (2 2 0) plane of InSb (JCPDS card No. 89-4299). These results further confirm that nanoinclusions at grain boundaries are InSb. In view of the structure–property correlation, these nanoinclusions at the grain boundaries are expected to profoundly affect TE properties.

3.2 Thermoelectric properties

Journal of Materials Chemistry C Accepted Manuscript

Journal of Materials Chemistry C Accepted Manuscript

The temperature dependent electrical conductivity and the Seebeck coefficient of all samples from 300 K to 800 K are shown in Figs. 5(a) and 5(b), respectively. In the temperature range studied, the electrical conductivity, on the order of 10^4 S/m, of all samples decreases gradually with increasing temperature, while the Seebeck coefficient, on the order of 10^2 μV/K, increases with increasing temperature. Both features are typical of a degenerate semiconductor. The Seebeck coefficients are positive in the temperature range investigated, indicative of *p*-type conduction. Regardless of the temperature, the electrical conductivity increases monotonously with increasing x, while the Seebeck coefficient exhibits an opposite trend. As shown in Fig. 5(b), the presence of InSb nanoinclusions moderately affects the power factor: the maximum power factors range from 1.7 to 1.9×10^{-3} $Wm^{-1}K^{-2}$.

To understand the underlying mechanism of the observed changes in the electronic transport properties, we conducted low temperature electrical conductivity and Hall coefficient measurements. The results are shown in the main panel and the upper-right inset of Fig. 5(c), respectively. The low temperature and high temperature electrical conductivity data were taken on the same sample, but the details of sample mounting as well as the measurement principle is different. Per our experience of measuring hundreds of samples, we usually take a 5% mismatch as normal. For comparison, the room temperature electrical conductivities for x = (0, 1, 3, 6, 10) samples are (8.8, 9.1, 9.2, 9.9, 8.6) × 10^4 S/m from low temperature apparatus and (8.9, 9.0, 9.4, 9.8, 10.1) × 10^4 S/m from high temperature measurement, i.e., a (1.1%, 1.1%, 2.1%, 1.0%, 14.8%) relative difference, respectively. Hence the mismatch

between the low temperature and high temperature electrical conductivity is generally acceptable in the present work except for the x=10 sample. In the x=10 sample, the InSb content is high so the characteristic length of composition inhomogeneity (the fluctuation between the host matrix phase and the nanophase) is not negligible any longer, the measurement result depends on the position of the voltage probe(s). In this case, the measurement data is still trustable but it is hard to directly compare the low temperature and high temperature data. The sign of the Hall coefficient is positive in the temperature range studied for all samples, confirming their *p*-type conduction mechanism. Carrier concentrations are nearly constant below 80 K and start to increase gradually thereafter. Notably, the presence of InSb nanoinclusions tends to decrease the room temperature carrier density, from ~ 3.4×10^{21} cm^{-3} for the x = 0 sample to ~ 1.6×10^{21} cm^{-3} for the x =10 sample.

One must bear in mind that the samples are nanocomposites, i.e., basically two -phase systems. In our case, the $FeSb_{2.2}Te_{0.8}$ host matrix is a degenerate *p*-type semiconductor while the pristine InSb tends to be an *n*-type non-degenerate semiconductor[36]. The chemical potential of a *p*-type degenerate semiconductor lies deep in its valence band while the chemical potential of an *n*-type non-degenerate semiconductor is usually close to the donor levels. A contact between a *p*-type material and an *n*-type material will initiate a charge transfer and create a depletion layer in-between. The voltage drop across the depletion layer will shift and align the chemical potential of the *p*-type and the *n*-type material (i.e., to satisfy the principle of detailed balancing).

Journal of Materials Chemistry C Accepted Manuscript

Journal of Materials Chemistry C Accepted Manuscript

Given the room temperature Seebeck coefficient value α ~ +100 μV/K, assuming a single free-electron parabolic band (the bipolar effect occurs above 700 K), we estimated that the chemical potential (μ) of $FeSb_{2.2}Te_{0.8}$ using the relationship $\alpha_p = (\frac{\pi^2}{3})(\frac{k_B}{e})\frac{(r+\frac{3}{2})}{(\frac{\epsilon_v-\mu}{k_BT})}$ for a p-type degenerate case[41], where k_B is the Boltzmann constant, ε_v the valence band edge energy, and r is the scattering parameter[42]. As shown in Fig 5(e), the Hall mobility near room temperature roughly follows a T^{1}behavior, suggesting a coexistence of acoustic phonon scattering (a $T^{-0.5}$ behavior) and charged defect scattering (a $T^{1.5}$ behavior). Choosing r = -1/2 for the acoustic phonon scattering mechanism yields a value of μ at about 73 meV below the valence band (V.B.) edge. Choosing r = 3/2 for the charge impurity scattering mechanism yields a value of μ at about 220 meV below the V.B. edge.

On the other hand, n-type InSb is a non-degenerate semiconductor[36] (see the inset in Fig. 5(f)), so its chemical potential lies close to the donor levels on the order of a few tens of meV below the conduction band (C.B.) edge.[43] Using the band gap E_g~ 0.25 eV for p-type $FeSb_{2.2}Te_{0.8}$ and ~ 0.18 eV for n-type InSb estimated from the Goldsmid-Sharp relationship ($E_g \approx 2e\alpha_{max}T_{max}$)[44], as well as the relative position of the chemical potential estimated above, we find that the occupied hole states in p-type $FeSb_{2.2}Te_{0.8}$ and the occupied electron states in n-type InSb likely overlap. As the thermal energy is 25 meV at room temperature, the overlap may become larger at elevated temperatures. As shown in Fig. 5(d), such overlap renders a “semimetal” like electronic behavior (even at temperatures well below the onset of the bipolar effect in each phase). This explains why the addition of n-type InSb nanoinclusions increases

the electrical conductivity but lowers the Seebeck coefficient.

With this understanding, we invoke a two-phase model to interpret the effective Seebeck coefficient. Recently, Gelbstein *et al.*[45] proposed a parallel configuration model to explain the Seebeck coefficient of the SnTe-Sn system based on the work of Bergman[46] and Levy[47] and general effective medium equations[48]. In this model, the effective Seebeck coefficient α_{eff} of an A-B composite (A, B represent the matrix and the second phase, respectively) is expressed as[45]:

$$\alpha_{\text{eff}}=\frac{\alpha_B\sigma_B\Phi+\alpha_A\sigma_A(1-\Phi)}{\sigma_B\Phi+\sigma_A(1-\Phi)} \quad (1)$$

where α_A and α_B denote the Seebeck coefficient of phase A and B, respectively and σ_A and σ_B designate the electrical conductivity of A and B phases. Φ stands for the volume fraction of component B. For the nominally x =1, 3, 6, and 10 samples, the results of the EPMA analysis yield the actual volume fraction of InSb as 0.4, 1.4, 2.9, and 4.6 vol.%, respectively. Using the data of Zhang *et al.*[36] for the electrical conductivity and the Seebeck coefficient of InSb (see the inset in Fig. 5(f)), the effective Seebeck coefficient α_{eff} of $FeSb_{2.2}Te_{0.8}$ with different InSb contents was estimated from Eq.1 and is presented in Fig. 5(f). Generally, the magnitude and the trend of the calculated Seebeck coefficient reproduce the observed results (Fig. 5(b)) fairly well.

The room temperature hole mobility (μ_H) is slightly increased by introducing 3 mol% of InSb nanoinclusions and increases further with the increasing InSb content (x). Namely, the room temperature hole mobility is 2.0, 2.2, 2.5 and 3.4 $cm^2V^{-1}s^{-1}$ for the x = 0, 3, 6, and 10 sample, respectively. This is different from most TE composites

Journal of Materials Chemistry C Accepted Manuscript

where the carrier mobility is usually degraded upon nanostructuring due to enhanced interfacial scattering.[36, 49-51] We attribute the increase in the carrier mobility of the $FeSb_{2.2}Te_{0.8}$/InSb composite to the presence of the high mobility InSb phase (for comparison, the room temperature mobility of InSb is ~2.3×10^4 $cm^2V^{-1}s^{-1}$)[36] at grain boundaries that serves as a conductive path across the grains (Fig. 3(f)), namely 'electron-channel'.

Thermal transport properties and *ZT* values for $FeSb_{2.2}Te_{0.8}$ - x% InSb (x = 0~10) composites are presented in Fig. 6. Above 300 K, as can be seen from Fig. 6(a), the total thermal conductivity decreases with increasing temperature (due to the Umklapp phonon-phonon scattering) until the onset of the bipolar effect resulting in notable upturns in the thermal conductivity. At low temperatures (2~100 K) as well as high temperatures (300~800 K), the total thermal conductivity decreases continuously with the increasing content of InSb in spite of slight increases in the electronic contribution. A notable exception is the x = 10 sample which, above 300 K, has a higher thermal conductivity than the x = 3 and x = 6 samples and, above 600 K, attains the highest thermal conductivity of all samples. Similarly, the thermal conductivity of the sample with the second highest InSb content, x = 6, exceeds the thermal conductivity of the x = 3 sample above 450 K, and even exceeds that of the x = 1 sample above 600 K. At this point, we speculate that this may be attributed to a percolation path in high InSb content samples. As a function of temperature, all samples show a distinct lattice thermal conductivity peak near 25 K (see the inset of Fig. 6(a)), characteristic of heat conduction in crystalline solids. The magnitude of the lattice thermal conductivity

Journal of Materials Chemistry C Accepted Manuscript

systematically decreases with the increasing content of InSb, which can be attributed to interfacial scattering of heat-carrying phonons at InSb nanoinclusions ('phonon-barrier' effect). The estimated high temperature lattice thermal conductivity for all samples is plotted in Fig. 6(b). The lattice thermal conductivity of binary $CoSb_3$[32], $FeSb_2Te$,[33] and $CeFe_4Sb_{12}$[7] is also included in the inset of Fig. 6(b) for comparison. Compared to $CoSb_3$, the lattice thermal conductivity of $FeSb_2Te$ is markedly decreased. For example, at room temperature, the lattice thermal conductivity of $FeSb_2Te$ is ~2.9 $Wm^{-1}K^{-1}$, only 30% of that of $CoSb_3$ (~10 $Wm^{-1}K^{-1}$). As a consequence of combined point defect scattering,[32, 33] mixed valence scattering[33], and interfacial scattering, the $FeSb_{2.2}Te_{0.8}$-6 mol.% InSb sample attains a very low κ_L of ~1 $Wm^{-1}K^{-1}$ at 800 K. This is the lowest value of the lattice thermal conductivity ever reported for an *unfilled* skutterudite compound and is close to that of fully filled $CeFe_4Sb_{12}$ (~ 0.7 $Wm^{-1}K^{-1}$) [7] at the same temperature.

Temperature dependent *ZT* values for all samples are displayed in Fig. 6(d). The presence of an appropriate amount of InSb nanoinclusions effectively boosts the TE performance of $FeSb_{2.2}Te_{0.8}$-based compounds over a wide temperature range. The highest figure of merit of ~ 0.76 at 800 K is achieved for the x = 3 sample, which represents about 15% improvement over the pristine sample and becomes comparable to the *ZT* of $CeFe_4Sb_{12}$. This enhancement in *ZT* mainly originates from the simultaneously enhanced carrier mobility and the reduced lattice thermal conductivity: the high mobility nanoinclusions uniformly distributed at grain boundaries can facilitate conductive channels (electron-channel) while also creating barriers to

Journal of Materials Chemistry C Accepted Manuscript

phonon propagation (phonon-barrier). This doping/nanocompositing approach can be utilized in other TE system and/or in combination with other established methods such as the traditional filling-rattling approach.

4. Conclusions

In summary, we synergistically enhanced the TE performance of *p*-type $FeSb_{2.2}Te_{0.8}$ by introducing *in-situ* formed InSb nanoinclusions. These nanoinclusions are of high mobility and disperse evenly at grain boundaries of the skutterudite matrix, facilitating conductive channels across the grains and thus enhancing the electrical conductivity (namely electron-channel). Meanwhile, the heat-carrying phonons are effectively impeded through enhanced interfacial scattering in conjunction with point defect scattering and mixed valence scattering (namely phonon-barrier). As a consequence, the highest ZT = 0.76 is achieved for the $FeSb_{2.2}Te_{0.8}$ nanocomposite with 3 mol.% InSb. This is a promising result because such performance of the unfilled skutterudite almost matches that of $CeFe_4Sb_{12}$, a well-known *p*-type filled skutterudite. Considering that the fabrication process of unfilled skutterudites is less complicated and less expensive than that of their filled cousins (many filler atoms are air- and moisture-sensitive), the high performance achieved with our p-type $FeSb_{2.2}Te_{0.8}$-based compounds has a considerable potential for industrial scale applications.

Acknowledgements

G. T. would like to thank Tingting Luo in the Materials Research and Test Center

Journal of Materials Chemistry C Accepted Manuscript

of WUT for the TEM study. This work was partially supported by the National Basic Research Program of China (Grant No. 2013CB632502), the Natural Science Foundation of China (Grant Nos. 51172174 and 51002112) and International Science & Technology Cooperation Program of China (Grant No. 2011DFB60150) along with 111 Project (Grant No. B07040). The work at the University of Michigan (low temperature transport studies) was supported by the Center for Solar and Thermal Energy Conversion, an Energy Frontier Research Center funded by the U.S. Department of Energy, Office of Science, Office of Basic Energy Science under Award Number DE-SC0000957. J. H. would like to thank the financial support of NSF DMR 1307740.

References

1. B. Sales, D. Mandrus and R. K. Williams, *Science*, 1996, **272**, 1325-1328.
2. B. Sales, D. Mandrus, B. Chakoumakos, V. Keppens and J. Thompson, *Phys. Rev. B*, 1997, **56**, 15081.
3. X. Shi, J. Yang, J. R. Salvador, M. Chi, J. Y. Cho, H. Wang, S. Bai, J. Yang, W. Zhang and L. Chen, *J. Am. Chem. Soc.*, 2011, **133**, 7837-7846.
4. G. Nolas, D. Morelli and T. M. Tritt, *Annu. Rev. Mater. Sci.*, 1999, **29**, 89-116.
5. W. Xie, J. He, H. J. Kang, X. Tang, S. Zhu, M. Laver, S. Wang, J. R. Copley, C. M. Brown and Q. Zhang, *Nano Lett.*, 2010, **10**, 3283-3289.
6. S. Wang, W. Xie, H. Li and X. Tang, *J. Phys. D: Appl. Phys.*, 2010, **43**, 335404.
7. G. Tan, S. Wang, H. Li, Y. Yan and X. Tang, *J. Solid State Chem.*, 2012, **187**, 316-322.
8. G. Tan, W. Liu, S. Wang, Y. Yan, H. Li, X. Tang and C. Uher, *J. Mater. Chem. A*, 2013, **1**, 12657-12668.
9. G. Tan, Y. Zheng and X. Tang, *Appl. Phys. Lett.*, 2013, **103**, 183904.
10. G. Rogl, A. Grytsiv, E. Royanian, P. Heinrich, E. Bauer, P. Rogl, M. Zehetbauer, S. Puchegger, M. Reinecker and W. Schranz, *Acta Mater.*, 2013, **61**, 4066-4079.
11. G. Rogl, A. Grytsiv, P. Rogl, N. Peranio, E. Bauer, M. Zehetbauer and O. Eibl, *Acta Mater.*, 2014, **63**, 30-43.
12. Y. Dong, P. Puneet, T. M. Tritt and G. S. Nolas, *J. Solid State Chem.*, 2014, **209**, 1-5.
13. G. Rogl, A. Grytsiv, P. Rogl, E. Bauer and M. Zehetbauer, *Intermetallics*, 2011, **19**, 546-555.
14. G. Rogl, A. Grytsiv, P. Rogl, E. Bauer, M. Kerber, M. Zehetbauer and S. Puchegger, *Intermetallics*, 2010, **18**, 2435-2444.

Journal of Materials Chemistry C Accepted Manuscript

15. D. Morelli, T. Caillat, J.-P. Fleurial, A. Borshchevsky, J. Vandersande, B. Chen and C. Uher, *Phys. Rev. B*, 1995, **51**, 9622-9628.
16. D. Mandrus, A. Migliori, T. Darling, M. Hundley, E. Peterson and J. Thompson, *Phys. Rev. B*, 1995, **52**, 4926-4931.
17. J. Feldman and D. Singh, *Phys. Rev. B*, 1996, **53**, 6273-6282.
18. G. Nolas, J. Cohn and G. Slack, *Phys. Rev. B*, 1998, **58**, 164.
19. M. M. Koza, M. R. Johnson, R. Viennois, H. Mutka, L. Girard and D. Ravot, *Nat. Mater.*, 2008, **7**, 805-810.
20. G. Nolas, M. Kaeser, R. Littleton IV and T. Tritt, *Appl. Phys. Lett.*, 2000, **77**, 1855-1857.
21. G. Nolas, G. Slack, D. Morelli, T. Tritt and A. Ehrlich, *J. Appl. Phys.*, 1996, **79**, 4002-4008.
22. G. S. Nolas, H. Takizawa, T. Endo, H. Sellinschegg and D. Johnson, *Appl. Phys. Lett.*, 2000, **77**, 52-54.
23. X. Shi, H. Kong, C.-P. Li, C. Uher, J. Yang, J. Salvador, H. Wang, L. Chen and W. Zhang, *Appl. Phys. Lett.*, 2008, **92**, 182101.
24. W. Zhao, P. Wei, Q. Zhang, C. Dong, L. Liu and X. Tang, *J. Am. Chem. Soc.*, 2009, **131**, 3713-3720.
25. L. Zhou, P. Qiu, C. Uher, X. Shi and L. Chen, *Intermetallics*, 2013, **32**, 209-213.
26. X. Shi, W. Zhang, L. Chen and J. Yang, *Phys. Rev. Lett.*, 2005, **95**, 185503.
27. H. Li, X. Tang, Q. Zhang and C. Uher, *Appl. Phys. Lett.*, 2009, **94**, 102114.
28. Z. Xiong, L. Xi, J. Ding, X. Chen, X. Huang, H. Gu, L. Chen and W. Zhang, *J. Mater. Res.*, 2011, **26**, 1848-1856.
29. J. W. Graff, X. Zeng, A. M. Dehkordi, J. He and T. Tritt, *J. Mater. Chem. A*, 2014, **2**, 8933-8940.
30. G. Tan, F. Shi, H. Sun, L.-D. Zhao, C. Uher, V. P. Dravid and M. G. Kanatzidis, *J. Mater. Chem. A*, 2014, **2**, 20849-20854.
31. G. Tan, F. Shi, S. Hao, H. Chi, L.-D. Zhao, C. Uher, C. Wolverton, V. P. Dravid and M. G. Kanatzidis, *J. Am. Chem. Soc.*, 2015, **137**, 5100-5112.
32. G. Tan, S. Wang and X. Tang, *Sci. Adv. Mater.*, 2013, **5**, 1974-1982.
33. G. Tan, W. Liu, H. Chi, X. Su, S. Wang, Y. Yan, X. Tang, W. Wong-Ng and C. Uher, *Acta Mater.*, 2013, **61**, 7693-7704.
34. M. Ohshita, *Jpn. J. Appl. Phys.*, 1971, **10**, 1365-1371.
35. D. Gaskill, G. Stauf and N. Bottka, *Appl. Phys. Lett.*, 1991, **58**, 1905-1907.
36. Q. Zhang, Z. Xiong, J. Jiang, W. Li, G. Xu, S. Bai, P. Cui and L. Chen, *J. Mater. Chem.*, 2011, **21**, 12398-12401.
37. K. Biswas, J. He, I. D. Blum, C.-I. Wu, T. P. Hogan, D. N. Seidman, V. P. Dravid and M. G. Kanatzidis, *Nature*, 2012, **489**, 414-418.
38. W. Xie, J. He, S. Zhu, X. Su, S. Wang, T. Holgate, J. Graff, V. Ponnambalam, S. Poon and X. Tang, *Acta Mater.*, 2010, **58**, 4705-4713.
39. J. Eilertsen, S. Rouvimov and M. Subramanian, *Acta Mater.*, 2012, **60**, 2178-2185.
40. J. Yu, W.-Y. Zhao, P. Wei, D.-G. Tang and Q.-J. Zhang, *J. Electron. Mater.*, 2012, **41**, 1414-1420.
41. G. S. Nolas, J. Sharp and H. J. Goldsmid, *Thermoelectrics: basic principles and new materials developments*, Springer, 2001.
42. W. F. Leonard and J. Thomas L. Martin, *Electronic Structure and Transport Properties of*

Journal of Materials Chemistry C Accepted Manuscript

Crystals, Krieger Publ. Co., Malabar, FL, 1979.
43. H. Miyazawa and H. Ikoma, *J. Phys. Soc. Jpn.*, 1967, **23**, 290-305.
44. H. Goldsmid and J. Sharp, *J. Electron. Mater.*, 1999, **28**, 869-872.
45. Y. Gelbstein, *J. Appl. Phys.*, 2009, **105**, 023713.
46. D. J. Bergman and O. Levy, *J. Appl. Phys.*, 1991, **70**, 6821-6833.
47. O. Levy and D. J. Bergman, *J. Phys. A: Math. Gen.*, 1992, **25**, 1875-1884.
48. D. S. McLachlan, M. Blaszkiewicz and R. E. Newnham, *J. Am. Ceram. Soc.*, 1990, **73**, 2187-2203.
49. G. Tan, L.-D. Zhao, F. Shi, J. W. Doak, S.-H. Lo, H. Sun, C. Wolverton, V. P. Dravid, C. Uher and M. G. Kanatzidis, *J. Am. Chem. Soc.*, 2014, **136**, 7006-7017.
50. X. Zhao, X. Shi, L. Chen, W. Zhang, S. Bai, Y. Pei, X. Li and T. Goto, *Appl. Phys. Lett.*, 2006, **89**, 092121.
51. A. Minnich, M. Dresselhaus, Z. Ren and G. Chen, *Energy Environ. Sci.*, 2009, **2**, 466-479.

Journal of Materials Chemistry C Accepted Manuscript

Figure captions

Figure 1. Powder XRD patterns of $FeSb_{2.2}Te_{0.8}$ - x mol.% InSb (x=0~10) nanocomposites.

Figure 2. FESEM images of freshly fractured surfaces of spark plasma sintered $FeSb_{2.2}Te_{0.8}$ - x mol.% InSb (x=0~10) nanocomposites: (a) x=0, (b) x=1, (c) x=3, (d) x=6, and (e) x=10; the red cycle in (b) highlights a few nanoinclusions at the grain boundaries of the x=1 sample; (f): more nanoinlcusions at the grain boundaries of the x=3 sample.

Figure 3. Microstructure and elemental distribution in the x=3 sample: (a) back scattered electron image (BSE), and EDS elemental mapping for Fe (b), Sb (c), In (d), Te (e). The white dotted line in (a) highlights the grain boundary. (f): a schematic diagram of the microstructure of the $FeSb_{2.2}Te_{0.8}$-InSb nanocomposite, in which the InSb-decorated grain boundaries facilitate electrical conduction but impede heat conduction.

Figure 4. (a) A typical TEM image for the x=3 sample; (b) HRTEM image for a nanoinclusion in (a); the inset of (b) shows an enlarged area in (b) for the measurement of the interplanar spacing of a nanoinclusion.

Figure 5. (a): Electrical conductivity and (b): Seebeck coefficient as a function of temperature for $FeSb_{2.2}Te_{0.8}$-x mol.% InSb (x=0~10) nanocomposites; the inset of (b): temperature dependent power factors; (c): low-temperature electrical conductivity data; the lower-left inset of (c) shows that low-temperature electrical conductivities match the high-temperature measurements fairly well; the upper-right inset of (c): temperature dependent carrier concentrations for the x=0, 3, 6, and 10 samples; (d) a schematic diagram of the electronic band structure of *p*-type $FeSb_{2.2}Te_{0.8}$ and *n*-type InSb in contact, where the humps labeled by h^+ and e^- represent the occupied 'hole' and 'electron' states, respectively. The solid curve lines denote the electron or hole density of states (DOS). The broken line curves stand for the Fermi-Dirac distribution functions $f_{F\text{-}D}$ of electrons (e^-) or holes (h^+), respectively. The occupied 'electron' or 'hole' states are a product of DOS and *f*. The chemical potential μ locates at f=1/2. The chemical potential of electron (μ_e) and that of hole (μ_h) align in accordance with the principle of "detailed balance". (e): temperature dependent Hall mobilities (μ_H) for the x=0, 3, 6, and 10 samples, two dotted lines represent a $\mu_H \sim T^{-1/2}$ behavior from charged impurity scattering and a $\mu_H \sim (T)^{-3/2}$ behavior from acoustic phonon scattering, respectively. A solid line $\mu_H \sim T^1$ is a better description of the observed temperature behavior of the mobility. (f) the calculated effective Seebeck coefficients as a function of temperature and x; the inset of (f): the electrical conductivity and Seebeck coefficient data of InSb[36] adopted in this study for the analysis of electrical transport data.

Figure 6. Temperature dependent thermal properties for $FeSb_{2.2}Te_{0.8}$-x mol.% InSb (x=0~10) nanocomposites (data with solid symbols are from high temperature

Journal of Materials Chemistry C Accepted Manuscript

measurement while those with open symbols are from low temperature measurement): (a) total thermal conductivity; (b) high temperature (above 300 K) lattice thermal conductivity. Inset of (a) shows the low temperature (below 300 K) lattice thermal conductivities of $FeSb_{2.2}Te_{0.8}$-InSb composites. Lattice thermal conductivities of a few skutterudite compounds ($CoSb_3$,[32] $FeSb_2Te$,[33] and $CeFe_4Sb_{12}$[7]) for comparison; (c) the lattice thermal conductivity as a function of x at 300 and 800 K, respectively; (d) temperature dependent *ZT* values for all samples in this study; the *ZT* data of $CeFe_4Sb_{12}$[7] is included for comparison.

Journal of Materials Chemistry C Accepted Manuscript

Table 1 Relative densities (ρ_R) and actual chemical compositions (CC) determined by EPMA for $FeSb_{2.2}Te_{0.8}$-x mol.% InSb.

x	0	1	3	6	10
ρ_R (%)	98.8	96.3	97.4	98.2	97.8
CC	$FeSb_{2.154}Te_{0.765}$	$FeSb_{2.164}Te_{0.759}In_{0.006}$	$FeSb_{2.178}Te_{0.778}In_{0.019}$	$FeSb_{2.201}Te_{0.767}In_{0.041}$	$FeSb_{2.224}Te_{0.747}In_{0.066}$

Journal of Materials Chemistry C Accepted Manuscript

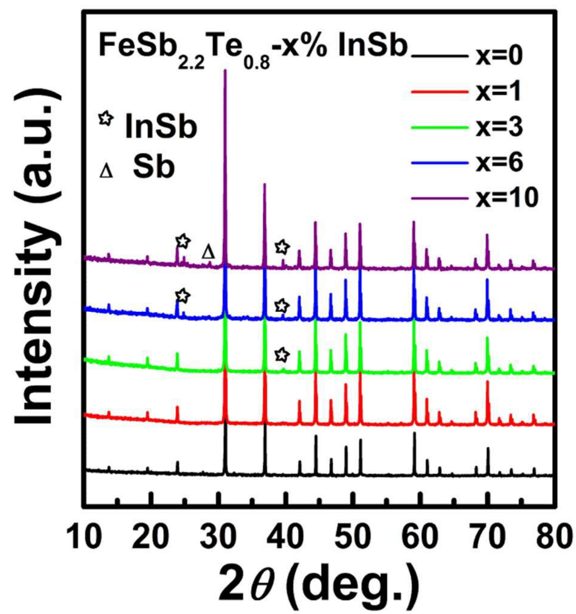

Figure 1

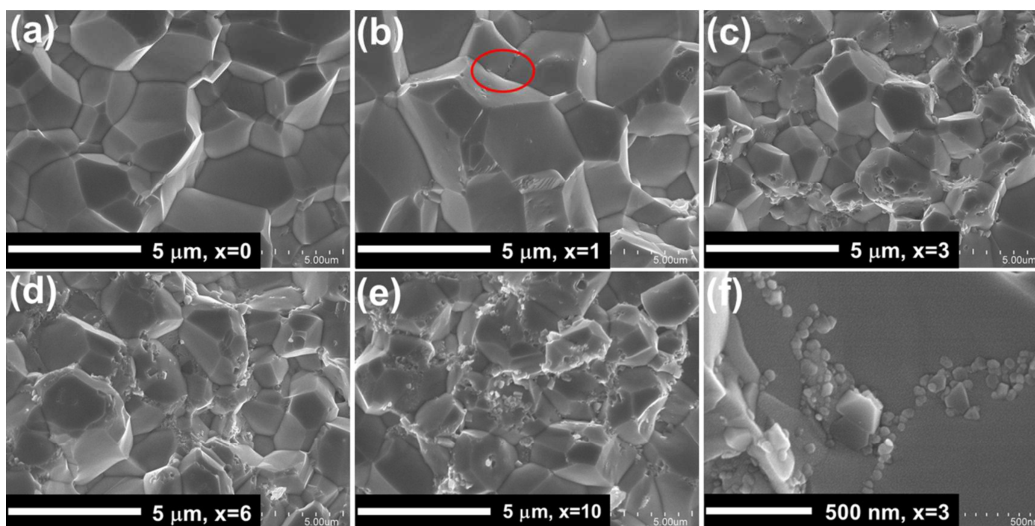

Figure 2

Journal of Materials Chemistry C Accepted Manuscript

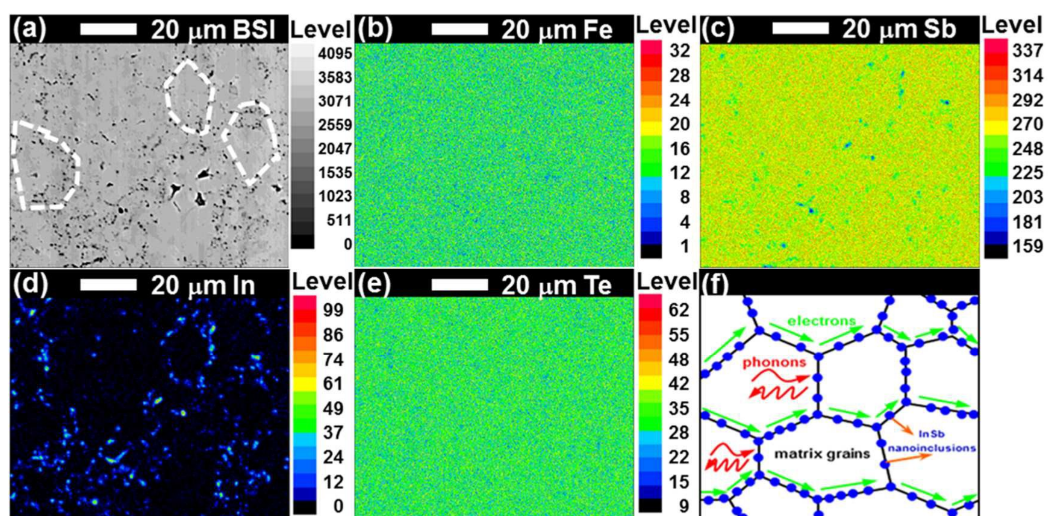

Figure 3

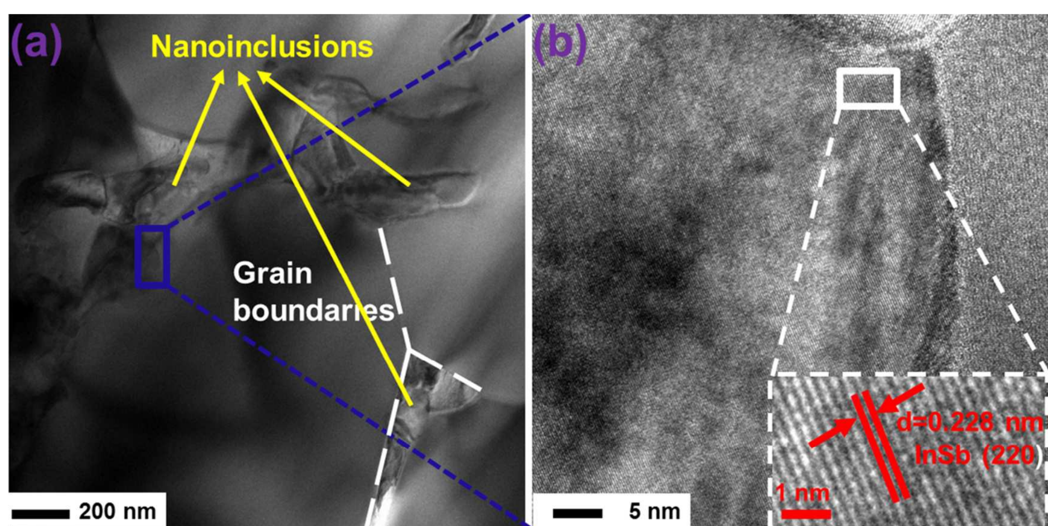

Figure 4

Journal of Materials Chemistry C Accepted Manuscript

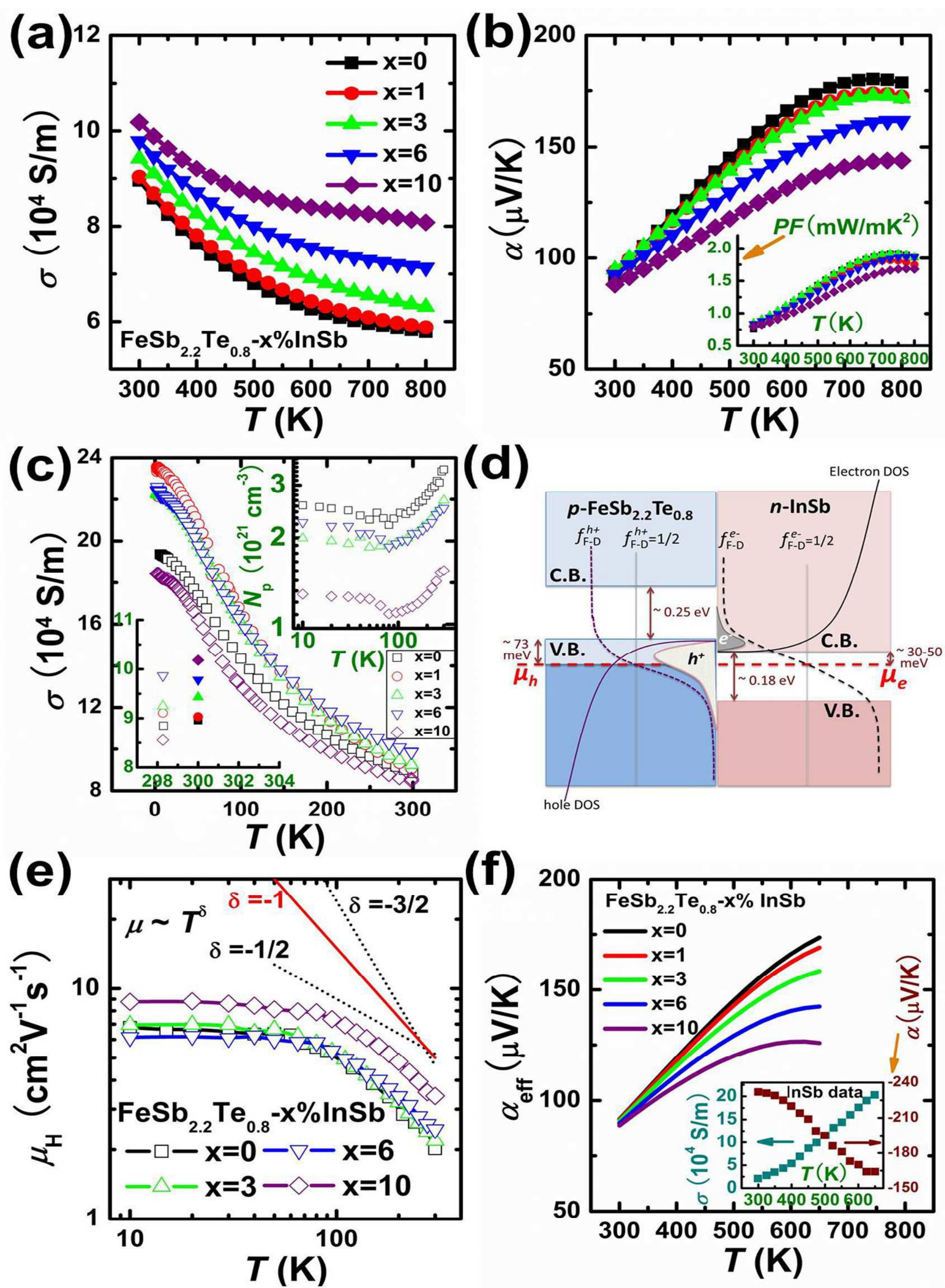

Figure 5

Journal of Materials Chemistry C Accepted Manuscript

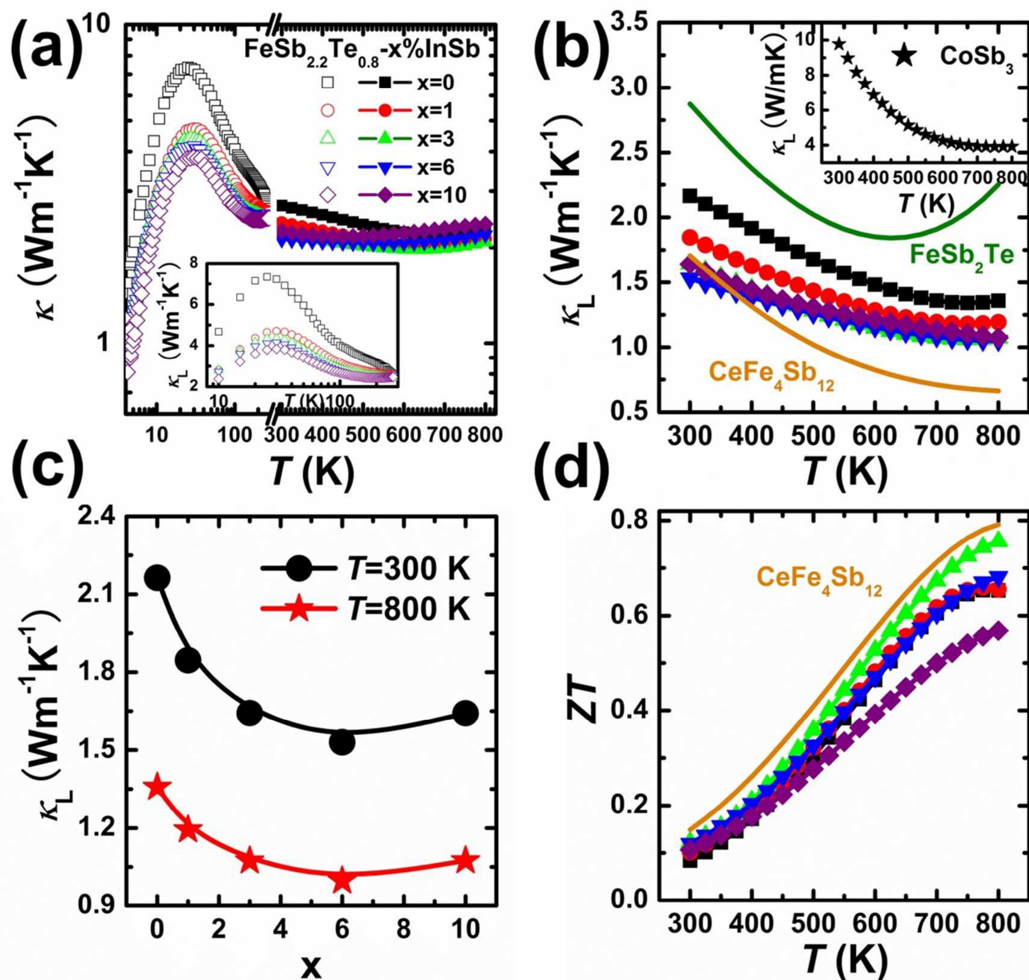

Figure 6

Journal of Materials Chemistry C Accepted Manuscript